# Observation of hydrodynamization and local prethermalization in 1D Bose gases

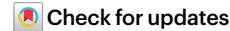
https://doi.org/10.1038/s41586-023-05979-9

Yuan Le<sup>1</sup>, Yicheng Zhang<sup>1</sup>, Sarang Gopalakrishnan<sup>1,2</sup>, Marcos Rigol<sup>1</sup> & David S. Weiss<sup>1⊠</sup>

Received: 7 October 2022

Accepted: 20 March 2023

Published online: 17 May 2023



Hydrodynamics accurately describe relativistic heavy-ion collision experiments well before local thermal equilibrium is established<sup>1</sup>. This unexpectedly rapid onset of hydrodynamics—which takes place on the fastest available timescale—is called hydrodynamization<sup>2-4</sup>. It occurs when an interacting quantum system is quenched with an energy density that is much greater than its ground-state energy density<sup>5,6</sup>. During hydrodynamization, energy gets redistributed across very different energy scales. Hydrodynamization precedes local equilibration among momentum modes<sup>5</sup>, which is local prethermalization to a generalized Gibbs ensemble<sup>7,8</sup> in nearly integrable systems or local thermalization in non-integrable systems<sup>9</sup>. Although many theories of quantum dynamics postulate local prethermalization<sup>10,11</sup>, the associated timescale has not been studied experimentally. Here we use an array of one-dimensional Bose gases to directly observe both hydrodynamization and local prethermalization. After we apply a Bragg scattering pulse, hydrodynamization is evident in the fast redistribution of energy among distant momentum modes, which occurs on timescales associated with the Bragg peak energies. Local prethermalization can be seen in the slower redistribution of occupation among nearby momentum modes. We find that the timescale for local prethermalization in our system is inversely proportional to the momenta involved. During hydrodynamization and local prethermalization, existing theories cannot quantitatively model our experiment. Exact theoretical calculations in the Tonks-Girardeau limit<sup>12</sup> show qualitatively similar features.

Hydrodynamization has been theoretically explored in high energy<sup>2-5,13,14</sup>, cosmological<sup>15</sup> and photo-excited correlated metal<sup>16</sup> contexts. These calculations typically involve simplified Hamiltonians that do not directly correspond to measurable physical systems. The process of hydrodynamization has not been directly observed in any system. We observe hydrodynamization using trapped one-dimensional (1D) Bose gases with point contact interactions (Lieb-Lininger (LL) gases<sup>17</sup>), quenching them with a Bragg pulse. The high energy density imparted by the pulse compared to the ground-state energy density of our ultracold gases allows us to realize this universal phenomenon. The near-integrability of trapped LL gases provides a framework from which we draw a general picture that applies to non-integrable systems.

As the strong coupling Tonks-Girardeau (TG) limit of our 1D Bose gases is exactly solvable, we first explain the physics of hydrodynamization and local prethermalization for a homogeneous TG gas. As we will see, our theoretical insights transfer to trapped systems with finite coupling such as the ones in the experiments. The TG Hamiltonian can be mapped onto non-interacting fermions by a change of variables that acts non-locally on the boson field operators. The prequench ground state is a Fermi sea, with a many-body wavefunction given by  $|\Psi_p\rangle = \prod_{|\theta| < \theta_F} \hat{c}_{\theta}^{\dagger} |0\rangle$ , where  $\hat{c}_{\theta}^{\dagger}$  creates a fermion with momentum  $\theta$  and  $\theta_{\rm F}$  is the Fermi momentum. Anticipating generalization to the finite-coupling regime, we will refer to the fermions as quasiparticles and their momenta as rapidities.

A Bragg pulse in the Raman–Nath regime transforms the initial wavefunction to  $|\Psi(t)\rangle = \prod_{|\theta|<\theta_{\rm F}} (\sum_n J_n(b) {\rm e}^{-{\rm i}t(\theta+n2\hbar k)^2/(2m\hbar)} \hat{c}_{\theta+n2\hbar k}^\dagger)|0\rangle$ , where  $k=2\pi/\lambda$ ,  $\lambda$  is the Bragg pulse wavelength, m is the atomic mass, t is time,  $2\pi\hbar$  is Planck's constant,  $J_i(b)$  are Bessel functions of the first kind, n is an integer and b depends on the Bragg pulse area  $^{18}$ . The rapidity distribution (which we denote as  $f(\theta)$ , see Fig. 1a) is conserved after the pulse<sup>7</sup>. The many-body wavefunction, on the other hand, evolves rapidly owing to the different phase factors associated with different quasiparticle rapidities. As the momentum distribution function of the bare particles (which we denote as f(p), see Fig. 1a) is determined by complicated multibody quasiparticle correlations of  $|\Psi(t)\rangle$  (Methods), relative phase evolution in the rapidity basis results in a change of occupancy of the momentum modes. The fastest rate at which f(p)can evolve is associated with the highest energy difference between significantly populated rapidity states and, consequently, results in a redistribution of energy among widely different momentum modes. This is the essence of hydrodynamization. For  $b \lesssim 1$ , the characteristic hydrodynamization frequency,  $\omega_{\rm hd}$ , is proportional to the energy difference between the n = 0 and  $\pm 1$  Bragg orders,  $\omega_{hd} = \hbar (2k)^2 / 2m$ . Figure 1b shows the evolution of f(p) on that fast timescale,  $T_{hd} = 2\pi/\omega_{hd}$ .

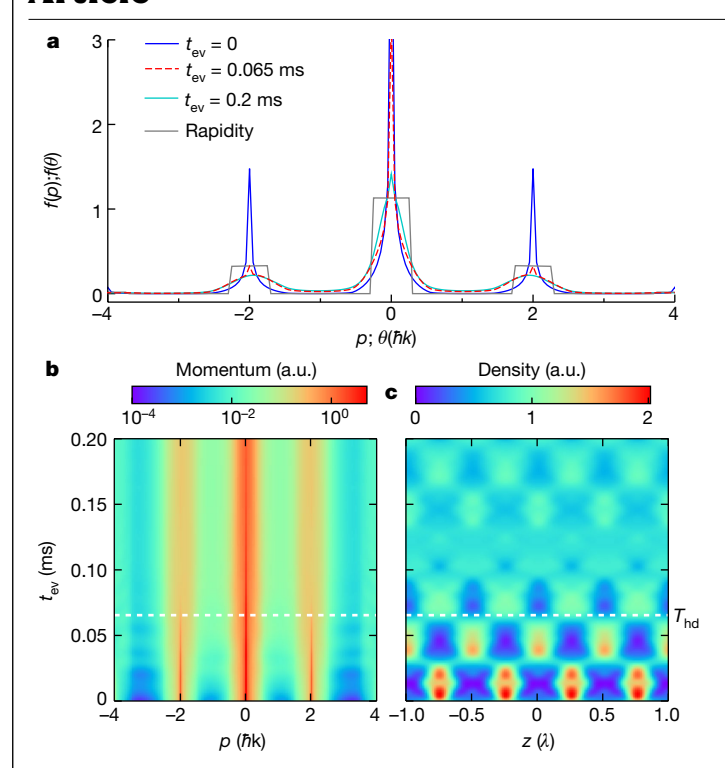
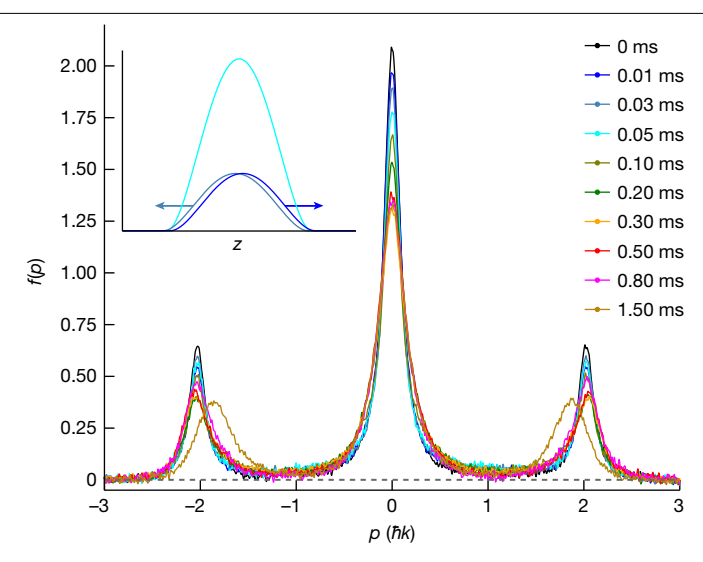


Fig. 1 | Evolution of a homogeneous TG gas after a Bragg quench.

**a**, Momentum and rapidity distributions. The grey curve is  $f(\theta)$ , which does not evolve. The blue curve is f(p) right after the quench. Relative phase evolution among rapidity states shows up as evolution of f(p). The red dashed curve shows f(p) after hydrodynamization. It differs from the blue curve largely by the transfer of energy from the side peaks to the modes between the peaks. The green curve shows f(p) after partial local prethermalization. It mostly only differs from the red curve in the vicinity of the peaks. **b**, Time evolution of f(p). The modes near  $\pm \hbar k$  are populated very rapidly because they are composed of the widest range of rapidities, which therefore dephase most rapidly, in approximately  $T_{hd}/(2\pi)$ . Closer to the momentum peaks, hydrodynamization is essentially complete by  $T_{\rm hd}$  (marked by a white dashed line). The slower change associated with local prethermalization can most easily be seen in the subtle later evolution of the central peak. c, Time evolution of the spatial density. The  $\lambda/2$  density oscillation in space (z) produced by the Bragg pulse is strongly reduced during hydrodynamization. The residual oscillations decay polynomially in time<sup>33,34</sup> and are unrelated to local prethermalization. Similar figures were presented in ref. 18 for larger b and in ref. 7 for a lattice quench. a.u., arbitrary units.

Because it happens so fast, the long-lived nature of the quasiparticles and the conservation of rapidities associated with integrability are not necessary for hydrodynamization. Non-integrable interacting many-body systems allow for a similar quasiparticle description on some short timescale. As long as the quench energy significantly exceeds the ground-state energy density, one expects that these quasiparticles will live much longer than the hydrodynamization timescale. So the above description of hydrodynamization applies.

The Bragg pulse quench provides a natural spatial view of hydrodynamization. It creates a  $\lambda/2$ -scale density oscillation (Fig. 1c), which tends to flatten on the timescale that the particles of the  $n=\pm 1$  side momentum peaks traverse  $\lambda/2$ ,  $(\lambda/2)/(2\hbar k/m)$ , that is, of the order of  $\pi/\omega_{\rm hd}$ . Viewed another way, the Bragg pulse creates two overlapped, oppositely directed, rapidly moving clouds that collide with each other and the stationary cloud. Hydrodynamization can occur even before the centre of masses of these clouds have traversed the average interparticle spacing. The collision energy, imparted with the creation of the Bragg peaks, is partially transferred to the momentum modes between the moving side peaks on hydrodynamization timescales (Fig. 1a,b; for



**Fig. 2** | **Evolving momentum distributions.** Each curve is the momentum distribution for  $\bar{y}_0 = 2.3$  at some time after the Bragg scattering quench. Before 0.5 ms, the side peaks have not yet noticeably been affected by the trap so they remain at their initial momenta. The insert is a sketch showing the spatial distribution and momenta of the atoms after the Bragg quench. It is like a collision that starts from complete overlap at t = 0.

a visualization of this experiment in a trap see the inset of Fig. 2). The situation is qualitatively similar in relativistic heavy-ion collisions, in which part of the kinetic energy in the centre of mass frame is rapidly redistributed from the colliding nuclei to the stationary emerging quark–gluon plasma. Quantitatively, the scale of collision energies in the two systems, which is inversely proportional to the timescale of hydrodynamization, differs by 18 orders of magnitude.

We call the evolution after hydrodynamization 'local prethermalization', during which the system approaches the local generalized Gibbs ensemble (GGE). Local thermalization has been studied in many cold atom experiments<sup>19</sup>, as has global prethermalization<sup>8,20,21</sup>, for which the local GGE remains satisfied while the entire system relaxes to a global (prethermal) equilibrium state. A Bragg pulse suddenly changes the many-body wavefunction and, even after hydrodynamization. the correlations in the many-body wavefunction have not yet locally equilibrated to the post-quench condition, the new local GGE. In the TG limit, the mapping to non-interacting fermions shows that f(p) is dominated by non-local correlations that involve fluctuations of the number of quasiparticles over a length scale  $\ell_p = 2\hbar\pi/p$  (Methods). Those fluctuations grow after the quench, as the fast quasiparticles in the  $n = \pm 1$  Bragg peaks (with velocities  $v_{+1} = \pm 2\hbar k/m$ ) move relative to the quasiparticles in the central peak. We expect the timescale for equilibration of f(p) to relate to the time it takes the fast quasiparticles to cross  $\ell_p$ ,  $\tau_p \approx \ell_p/|v_{+1}| = \pi m/(pk)$ . Hence, after a Bragg pulse, local prethermalization of the bosonic momentum distribution occurs on timescales that are inversely proportional to p and k. Beyond the TG limit, this is expected to hold true in general for nearly integrable 1D systems with long-lived quasiparticles, as in our experimental setup<sup>22,23</sup>. Using the local density approximation, it also applies to trapped systems at least as long as the density profile does not change significantly during local prethermalization.

Our experiment starts with a bundle of nearly zero temperature 1D gases consisting of <sup>87</sup>Rb atoms confined in a blue-detuned two-dimensional (2D) lattice, with axial trapping provided by crossed red-detuned dipole trapping beams (Methods). We pulse on an axial lattice beam with wavevector  $k_0 = 2\pi/(775 \text{ nm})$  for 6 µs and then measure the momentum distribution (Methods) as a function of the time  $t_{\rm rev}$  after the pulse. Bragg pulses have previously been used with 1D gases

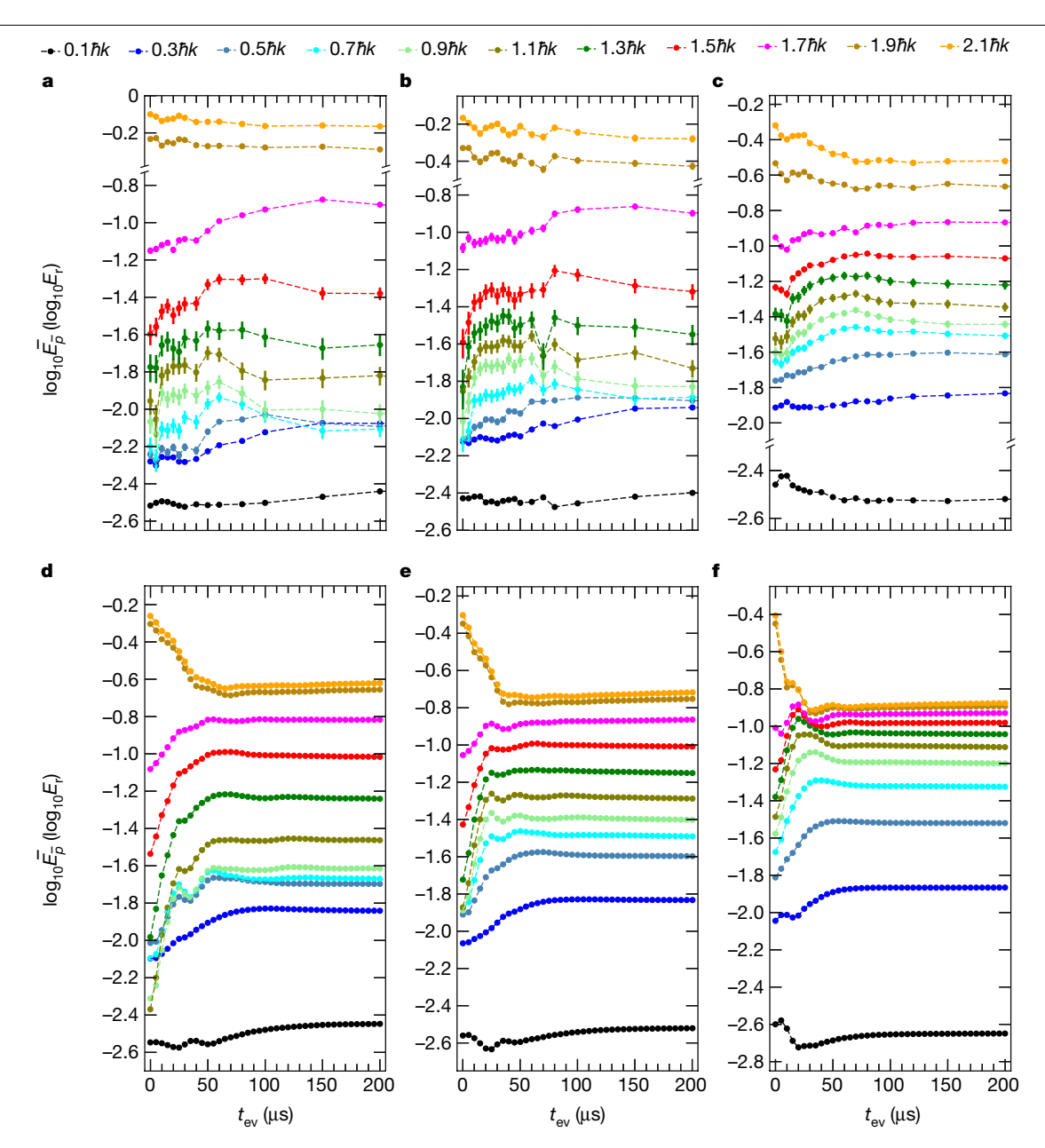
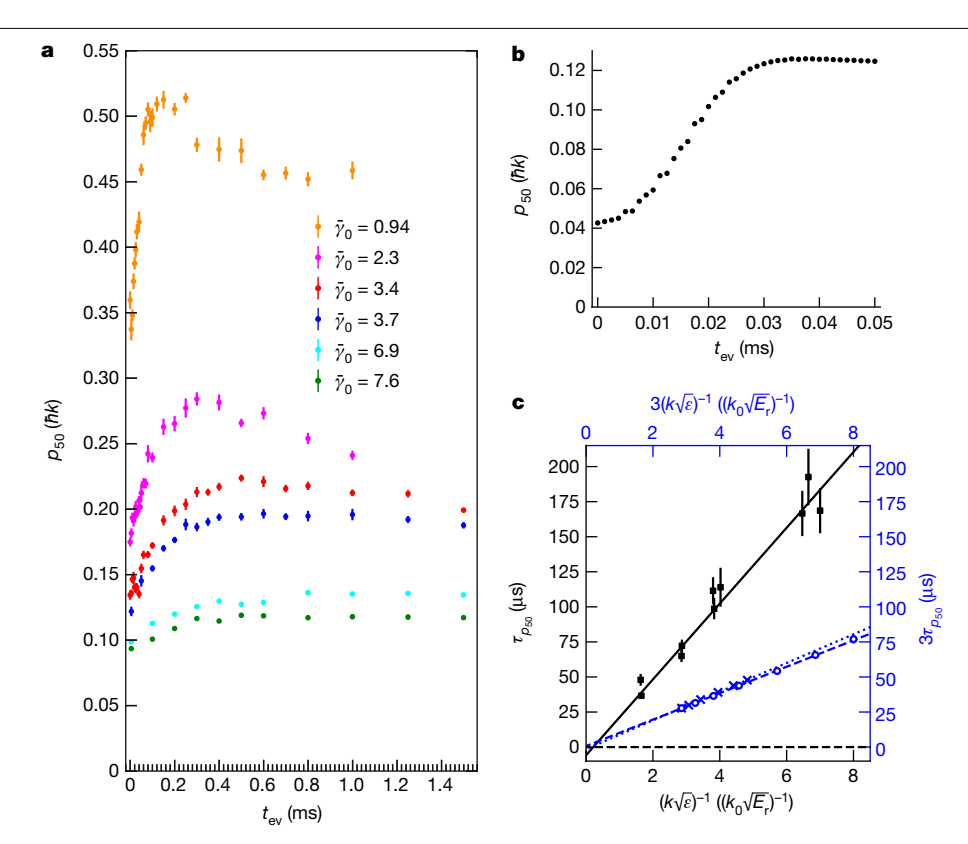


Fig. 3 | Hydrodynamization. Each curve is the time evolution of the integrated energy in a different  $0.2\hbar k_0$  wide momentum group. The central momentum of each colour-coded group is shown in the legend.  $\mathbf{a} - \mathbf{c}$ , Experimental curves for  $\overline{\gamma}_0 = 3.4$  (a), 2.3 (b) and 0.94 (c). See Methods for an explanation of the error bars. **d**-**f**, Theoretical curves for single 1D gases in the TG-gas limit. The average energies per particle of the three theory figures are the same as the experimental  $figures \, immediately \, above \, them \, in \, {\color{red} a-c}, respectively. \, Hydrodynamization \, is \,$ 

evident in the approximately 33 µs period oscillations of the few lowest and highest momentum groups in each figure. The most dramatic feature of hydrodynamization is the very rapid initial energy changes in the intermediate momentum groups. Variations among the different experimental and theoretical figures are discussed in the text. The dashed lines are guides to the eye.

to prepare quantum Newton's cradles 20,24,25 and to measure dynamical structure factors<sup>26,27</sup>. Figure 2 shows a set of momentum distributions for an initial (pre-Bragg pulse) weighted average dimensionless interaction strength,  $\bar{\gamma}_{0}$ , of 2.3 (Methods). The curves range over the first 1.5 ms, which is short compared with the axial oscillation period of 16.7 ms. The expected Bragg side peaks are visible, as is their eventual slowing down (see the 1.5 ms curve) due to the axial trap. In what follows we focus on short times, for which the side peaks are not significantly affected by the presence of the trap and remain at their initial momenta. Corresponding TG theory curves are shown in Extended Data Fig. 1.

Hydrodynamization causes rapid changes in the energy distribution of the system. To see it, we integrate the kinetic energy in successive momentum ranges (denoted by their average momentum,  $\overline{p}$ ) and plot those integrated energies as a function of time in units of the recoil energy,  $E_r = (\hbar k_0)^2 / 2m$ . Experimental data for momentum groups up to the first Bragg peak are shown in Fig. 3a–c for  $\overline{\gamma}_0$ =3.4, 2.3 and 0.94, respectively. Results from TG-gas theory are shown in Fig. 3d-f, for single 1D gases with the same average energy per particle as the experimental curves in Fig. 3a-c. The early time dynamics are due to hydrodynamization. Extended Data Figs. 2 and 3 show the evolution of the experimental rapidity distribution for  $\overline{y}_0 = 2.3$  and the theoretical TG rapidity distribution with the same average rapidity energy, respectively (see also ref. 18). Extended Data Fig. 4 shows the rapidities version of Fig. 3b. As expected, the rapidity distribution does not evolve on these timescales.



**Fig. 4** | **Local prethermalization. a**, For a range of  $\bar{\gamma}_0$  we plot  $p_{50}$ , the momentum line dividing the atoms in the central peak in half, as a function of the time after the Bragg pulse. The different coloured curves correspond to different experimental  $\overline{y}_{0}$ , as shown in the key. Local prethermalization is essentially complete by the time each curve reaches its peak. The slow decreases in  $p_{50}$ after local prethermalization results from the Bragg side peaks gradually separating from the centre peak, so that the local GGE slowly evolves throughout the gas. TG-gas calculations, for which we have access to the spatial distributions, confirm this understanding. **b**, A typical TG theory  $p_{50}(t_{ev})$  curve. The result is for a single 1D gas with  $k = 4k_0$  and a peak 1D density of 1.36 ( $\mu$ m)<sup>-1</sup>. Small hydrodynamization oscillations are just barely visible throughout local prethermalization in the theory. c, Local prethermalization timescales versus

 $(k\sqrt{\epsilon})^{-1}$ . The black experimental points show the time constants extracted from curves such as those in **a**. As for all the experimental data,  $k = k_0$  for this curve. See Methods for an explanation of the error bars. The blue points use the upper and right axes, and show the time constants extracted from curves such as those in **b** for a fixed  $k = 4k_0$  (crosses) or a fixed  $\epsilon = 0.06885\hbar k_0$  (open circles). The solid, dotted and dashed lines are least-squares fits to the associated points; all the intercepts are zero to within a few standard deviations  $(-5.8 \pm 4.9, -0.47 \pm 0.13, 0.25 \pm 0.081$  for the black squares, blue crosses and blue circles, respectively). These results validate our qualitative model, which says that the local prethermalization rate scales inversely with p and the Bragg peak velocity. The slope of the experimental line is 2.6 times the slope of the theory lines.

The details of Fig. 3 cannot be predicted without a dynamical model that can be solved at finite coupling after this strong quench. From the experimental results, several general observations can be made. Figure 3b is the clearest experimental result to interpret, as it is at a 'sweet spot' where the three dominant momentum peaks are well resolved but the occupation of the intermediate momentum modes is not too small. The  $\overline{p}$  = 1.9 and 2.1 curves show an oscillation period of approximately  $T_{\rm hd}/2 = 33 \,\mu \text{s}$ , and the  $\overline{p} = 0.1$ , 0.3 and 0.5 curves show an out of phase oscillation. The momentum oscillation period is half the spatial oscillation period seen in Fig. 1c, presumably because the phase of the underlying density distribution does not affect the momentum occupancies. The intermediate curves from  $\overline{p} = 0.7$  to 1.5 all show a rapid rise with a characteristic time of approximately  $(T_{hd}/2)/\pi$ . These momentum modes must draw from a very wide range of rapidity modes in both the central and side peaks for the dephasing to occur so rapidly.

Figure 3a has qualitatively similar hydrodynamization features to Fig. 3b. The  $\omega_{hd}$  oscillations of the side momentum peak ( $\overline{p}$  = 1.9 and 2.1) are less pronounced than in Fig. 3b, indicating that the central peak rapidities play less of a role there. The intermediate  $\overline{p}$  curves also rise rapidly. As in Fig. 3b, they must draw from a wide range of rapidity components, but they have more oscillations with  $T_{\rm hd}/2$ ; this seems reasonable given the narrower rapidity distributions of each peak and correspondingly slower dephasing times. The dephasing in Fig. 3c is faster in all momentum curves, which is a consequence of wider rapidity distributions. In the intermediate  $\overline{p}$  curves, hydrodynamization manifests as rapid initial downturns.

The various hydrodynamization features of the TG-gas theory shown in Fig. 3d-f are similar to those in the associated experiments. One would not expect them to be identical because the mapping between rapidities and momenta are different for different values of  $\gamma$ . The hydrodynamization timescale is predictably the same for all these results, and the hydrodynamization dephasing times are qualitatively similar for experiment and theory curves with the same rapidity energy per particle (those in the same column). The biggest difference between the theory and experiment (other than the absence of noise in the theory) is that the energy changes during hydrodynamization are about 2.5 times greater in the theory. One can perhaps qualitatively understand this because the prequench kinetic energy in our experimental range of  $\bar{y}_0$  ranges from 20% to 65% of the rapidity energy, with the rest being interaction energy. For infinite  $\gamma$ , all the energy is kinetic. The rapid initial decay of the  $\overline{p}$ =1.9 and 2.1 peaks in the theory may also relate to the absence of interaction energy. Qualitative differences with the experiment are not finite temperature effects (Extended Data Fig. 5).

The onset of local prethermalization is also visible in Fig. 3. After hydrodynamization dephasing is complete, which takes approximately  $T_{\rm hd}$  (approximately 65 µs) for all curves, the energies continue to evolve, approaching their GGE values on progressively longer timescales as the momentum decreases. This can be most clearly seen in the theory (Fig. 3d-f) and in the lower  $\bar{y}_0$  experimental results (Fig. 3c), looking from the  $\overline{p}$  = 1.5 to 0.3 curves in each panel. Local prethermalization is more than twice as fast in the theory than it is in the experiments with the same rapidity energy. It is, however, difficult to consistently extract local prethermalization time constants because of the diversity of curve shapes and the modest separation of hydrodynamization and local prethermalization timescales in this momentum range.

To better study local prethermalization, we focus on the redistribution among momentum modes for which the occupations are large and vary rapidly with momentum. We find a robust observable in the momentum dividing line,  $p_f$  between the f% of lower momentum atoms in the central peak (between  $-\hbar k_0$  and  $+\hbar k_0$ ) and the rest. Here f = 50selects a momentum near the full-width at half-maximum of the central peak. Figure 4a shows a set of experimental  $p_{50}$  curves as a function of time (see Extended Data Figs. 6 and 7 for curves that show other possible observables). We extract  $\tau_{n_{co}}$  from each of the curves in Fig. 4a by finding the time at which  $p_{50}$  is half way between its initial and peak values (Methods).

In Fig. 4c, we plot  $\tau_{p_{s_0}}$  for a range of  $\overline{\gamma_0}$ , choosing the abscissa to be  $1/\sqrt{\epsilon_0}$ , where  $\epsilon_0$  is the calculated average prequench energy per particle from LL theory. The data fit to a straight line with an intercept close to zero. We also find that  $p_{50}$  at the midpoint of local prethermalization,  $p_{50}^{\rm m}$ , is proportional to  $\sqrt{\varepsilon_0}$  (Extended Data Fig. 8). Qualitatively, we expect  $\tau_{p_{s_0}}$  to be inversely proportional to the effective momentum being measured, which we will call  $\overline{p}_{50}$ . The linear fits in Fig. 4c and Extended Data Fig. 8 together strongly imply that both  $\sqrt{\varepsilon_0}$  and  $p_{50}^{\rm m}$  are proportional to  $\overline{p}_{50}$ , so that the local prethermalization rate is in fact inversely proportional to momentum. The linear fits also work well for f = 40 and 60 (Extended Data Fig. 8a,c), although the ratio of  $\overline{p}_{f}$  to  $p_{f}^{m}$ depends on f.

Because the hydrodynamization features in the theory are larger and local prethermalization is faster, we calculate  $p_{50}$  for simulations with  $k = 4k_0$  to achieve a better separation of timescales  $(1/\omega_{hd} \propto 1/k^2)$ while  $\tau_{p_{s_0}} \propto 1/k$ ). An example of  $p_{s_0}(t_{e_v})$  is shown in Fig. 4b and the theoretical results for  $au_{p_{50}}$  versus  $1/\sqrt{\epsilon}$  are the blue crosses in Fig. 4c. The linear fit crosses the axes near the origin, as in the experiment. The blue open circles show  $\tau_{p_{so}}$  versus 1/k. The fact that its linear fit also nearly crosses the origin validates the velocity part of our dimensional argument. While both experiment and theory show that  $au_{p_{50}} = C/(k\sqrt{\epsilon})$ , the associated constant C differs for the two. Specifically,  $C_{\text{exp}} = 2.6C_{\text{thr}}$ which is consistent with the results in Fig. 3. The difference in C is presumably related to the difference in the strength of  $\delta$ -function interactions, which has a fixed, finite value in the experiment and is infinite in the theory. (It is neither due to temperature effects nor to the average over 1D gases (Extended Data Fig. 9)). The time for the TG gas to reach the local GGE is about twice  $\tau_{p_{s_0}}$  (Fig. 4b), which we find is approximately five times faster than the time it takes the Bragg scattered components to traverse the wavelength associated with  $p_{50}^{\rm m}$ 

We have used nearly integrable 1D Bose gases to explain the behaviour of many-body quantum systems immediately after a rapid, high-energy quench. There are two distinct timescales. The first is hydrodynamization, during which short distance variations in the wavefunctions smooth out and energy is rapidly redistributed among distant momentum modes. Although hydrodynamization is qualitatively the same in a wide range of many-body quantum systems, it is easier to study with cold atoms because one can rapidly shut off interactions and thus measure evolving momentum distributions with good time resolution. The second is local prethermalization, which in our experiment involves a redistribution among nearby momentum modes on timescales that vary inversely with momentum. We find that local prethermalization is surprisingly fast. For nearly integrable systems such as the trapped LL gas, the system approaches the local GGE during local

prethermalization. Local prethermalization can also occur in far from integrable systems when there are extra conserved quantities<sup>10</sup>.

Outside of the hard-core limit, no existing theory can calculate the complete dynamics during hydrodynamization and local prethermalization, which makes it an important frontier of many-body dynamical theory. Generalized hydrodynamics (GHD) was developed to calculate the local dynamics of the rapidity distribution, with the assumption of local equilibration to the GGE<sup>23,28-30</sup>. GHD is only concerned with the spatially resolved rapidity distribution,  $n(\theta, z)$ . After the quench, the rapidity distribution does not change until the side peaks start to climb the trap potential, which happens after local prethermalization (Fig. 2 and Extended Data Fig. 2). The short distance density oscillations are strongly reduced during hydrodynamization (Fig. 1c), so the spatial distribution is nearly constant during local prethermalization. Therefore,  $n(\theta, z)$  does not change during local prethermalization despite the fact that f(p) changes; a GHD calculation that starts right after hydrodynamization will accurately describe the ensuing dynamics in the trap.

There is a strong parallel between our experiment and relativistic heavy-ion collisions, for which hydrodynamics is also valid after hydrodynamization. There are, however, two qualitative differences. First, hydrodynamic quantities evolve during local thermalization in relativistic heavy-ion collisions. How accurate GHD remains when  $n(\theta, x)$ varies during local prethermalization, and how GHD might need to be improved if it is not, is an open question that can be studied with quenches in much tighter traps, both theoretically for the TG gas and experimentally for all y. Second, nuclear matter is far from integrable. Additional experimental work can shed more light on why and the extent to which hydrodynamic descriptions apply during local thermalization. Bragg scattering quenches in unitary three-dimensional gases may be good candidates for such studies, as these gases have been shown to locally thermalize on short and controllable timescales<sup>31,32</sup>.

#### **Online content**

Any methods, additional references, Nature Portfolio reporting summaries, source data, extended data, supplementary information, acknowledgements, peer review information; details of author contributions and competing interests; and statements of data and code availability are available at https://doi.org/10.1038/s41586-023-05979-9.

- Rapp, R. Theory highlights of quark matter 2004. J. Phys. G Nucl. Part. Phys. 30, S951-S961
- Florkowski, W., Heller, M. P. & Spaliński, M. New theories of relativistic hydrodynamics in the LHC era. Rep. Prog. Phys. 81, 046001 (2018).
- Schenke, B. The smallest fluid on earth. Rep. Prog. Phys. 84, 082301 (2021).
- Berges, J., Heller, M. P., Mazeliauskas, A. & Venugopalan, R. Qcd thermalization: ab initio approaches and interdisciplinary connections, Rev. Mod. Phys. 93, 035003 (2021)
- Berges, J., Borsányi, S. & Wetterich, C. Prethermalization. Phys. Rev. Lett. 93, 142002 (2004).
- Borsanyi, S. Prethermalization and the first 1 fm/c of a heavy ion collision. Acta Phys. Hung, A 22, 317-323 (2005).
- Rigol, M., Dunjko, V., Yurovsky, V. & Olshanii, M. Relaxation in a completely integrable many-body quantum system: an Ab Initio study of the dynamics of the highly excited states of 1D lattice hard-core bosons, Phys. Rev. Lett. 98, 050405 (2007)
- Gring, M. et al. Relaxation and prethermalization in an isolated quantum system. Science 337. 1318–1322 (2012).
- D'Alessio, L., Kafri, Y., Polkovnikov, A. & Rigol, M. From quantum chaos and eigenstate thermalization to statistical mechanics and thermodynamics. Adv. Phys. 65, 239-362 (2016).
- 10. Mallayya, K., Rigol, M. & De Roeck, W. Prethermalization and thermalization in isolated quantum systems. Phys. Rev. X 9, 021027 (2019).
- Doyon, B. Lecture notes on generalised hydrodynamics. SciPost Phys. Lect. Notes https:// doi.org/10.21468/SciPostPhysLectNotes.18 (2020).
- Girardeau, M. Relationship between systems of impenetrable bosons and fermions in one dimension. J. Math. Phys. 1, 516-523 (1960).
- Heller, M. P. & Spaliński, M. Hydrodynamics beyond the gradient expansion: resurgence and resummation, Phys. Rev. Lett. 115, 072501 (2015).
- Giacalone, G., Mazeliauskas, A. & Schlichting, S. Hydrodynamic attractors, initial state energy, and particle production in relativistic nuclear collisions. Phys. Rev. Lett. 123,
- Cooper, F., Habib, S., Kluger, Y. & Mottola, E. Nonequilibrium dynamics of symmetry breaking in λΦ<sup>4</sup> theory. Phys. Rev. D 55, 6471-6503 (1997).

- Alexander, M. & Kollar, M. Photoinduced prethermalization phenomena in correlated metals. Phys. Status Solidi B 259, 2100280 (2022).
- 17. Lieb, E. H. & Liniger, W. Exact analysis of an interacting Bose gas. I. The general solution and the ground state. Phys. Rev. 130, 1605-1616 (1963).
- van den Berg, R. et al. Separation of time scales in a quantum Newton's cradle. Phys. Rev. Lett. 116, 225302 (2016).
- Gross, C. & Bloch, I. Quantum simulations with ultracold atoms in optical lattices. Science **357**, 995-1001 (2017).
- 20. Kinoshita, T., Wenger, T. & Weiss, D. S. A quantum Newton's cradle. Nature 440, 900-903
- Langen, T., Gasenzer, T. and Schmiedmayer, J. Prethermalization and universal dynamics in near-integrable quantum systems. J. Stat. Mech. https://doi.org/10.1088/1742-5468/ 2016/06/064009 (2016).
- Wilson, J. M. et al. Observation of dynamical fermionization. Science 367, 1461–1464 (2020).
- Malvania, N. et al. Generalized hydrodynamics in strongly interacting 1D bose gases. Science 373, 1129-1132 (2021).
- Tang, Y. et al. Thermalization near integrability in a dipolar quantum newton's cradle. 24. Phys. Rev. X 8, 021030 (2018).
- Li, C. et al. Relaxation of bosons in one dimension and the onset of dimensional crossover. SciPost Phys. 9, 058 (2020).
- Fabbri, N. et al. Dynamical structure factor of one-dimensional bose gases: experimental signatures of beyond-luttinger-liquid physics. Phys. Rev. A 91, 043617 (2015).
- Meinert, F. et al. Probing the excitations of a lieb-liniger gas from weak to strong coupling. Phys. Rev. Lett. 115, 085301 (2015).

- 28. Castro-Alvaredo, O. A., Doyon, B. & Yoshimura, T. Emergent hydrodynamics in integrable quantum systems out of equilibrium. Phys. Rev. X 6, 041065 (2016).
- 29. Bertini, B., Collura, M., De Nardis, J. & Fagotti, M. Transport in out-of-equilibrium XXZ chains: exact profiles of charges and currents. Phys. Rev. Lett. 117, 207201 (2016).
- 30. Schemmer, M., Bouchoule, I., Doyon, B. & Dubail, J. Generalized hydrodynamics on an atom chip. Phys. Rev. Lett. 122, 090601 (2019).
- Eigen, C. et al. Universal prethermal dynamics of bose gases quenched to unitarity. Nature **563**, 221-224 (2018).
- 32. Yin, X. & Radzihovsky, L. Quench dynamics of a strongly interacting resonant bose gas. Phys. Rev. A 88, 063611 (2013).
- 33. Gramsch, C. & Rigol, M. Quenches in a quasidisordered integrable lattice system: dynamics and statistical description of observables after relaxation. Phys. Rev. A 86, 053615 (2012).
- 34. Murthy, C. & Srednicki, M. Relaxation to Gaussian and generalized Gibbs states in systems of particles with quadratic Hamiltonians. Phys. Rev. E 100, 012146 (2019).

Publisher's note Springer Nature remains neutral with regard to jurisdictional claims in published maps and institutional affiliations.

Springer Nature or its licensor (e.g. a society or other partner) holds exclusive rights to this article under a publishing agreement with the author(s) or other rightsholder(s); author self-archiving of the accepted manuscript version of this article is solely governed by the terms of such publishing agreement and applicable law.

© The Author(s), under exclusive licence to Springer Nature Limited 2023

#### Methods

#### **Experimental setup**

We create a Bose–Einstein condensate of <sup>87</sup>Rb in the F = 1,  $m_f = 1$  ground state by evaporative cooling in a compressible red-detuned crossed dipole trap made with 1,064 nm wavelength light and final beam waists of 57 µm (ref. 35). We control the atom number in the Bose-Einstein condensate, which ranges from  $2 \times 10^5$  to  $3.4 \times 10^5$  atoms, by varying the final evaporation depth of the crossed dipole trap. We then ramp up the crossed dipole trap to powers that range from 5.8 to 157 mW, which allows us to start with a range of initial trap densities. We next create a bundle of 1D gases by adiabatically ramping up a blue-detuned  $40E_r$ -deep 2D lattice made with diameter 432 µm, power 139 mW, wavelength 775 nm, retroreflected pairs of crossed beams. For our Bragg scattering experiment, we pulse on a similar axial lattice beam pair. The lattice and Bragg beam pairs are all mutually offset from each other by radio frequencies to prevent mutual interference. The depth of the Bragg lattice is  $27E_r$ . During the 6 µs pulse, the incipient first momentum sidebands move approximately 70 nm, which is not negligibly small compared with the lattice period of 387.5 nm. The evolution of the system during the pulse slightly modifies the shape and relative peak heights of the rapidity distributions compared to a shorter pulse on a non-interacting gas, but the difference is qualitatively unimportant to the postpulse evolution that we study in this Article.

#### Lieb-Liniger model

The experimental system can be modelled as a 2D array of independent 1D gases. Each 1D gas is described by the LL Hamiltonian in the presence of a confining potential U(z) (ref. 17),

$$\mathcal{H}_{LL} = \sum_{j=1}^{N} \left[ -\frac{\hbar^2}{2m} \frac{\partial^2}{\partial z_j^2} + U(z_j) \right] + g \sum_{1 \le j < l \le N} \delta(z_j - z_l), \tag{1}$$

where m is the mass of a <sup>87</sup>Rb atom and N is the number of atoms. g (>0 in our case) is the strength of the effective 1D contact interaction, which depends on the depth of 2D lattice<sup>36</sup>. In the absence of a confining potential U(z), Hamiltonian (1) is exactly solvable via the Bethe ansatz<sup>17,37</sup>. All observables in the equilibrium states depend only on the dimensionless coupling strength  $\gamma = mg/n_{\rm 1D}\hbar^2$ , where  $n_{\rm 1D}$  is the particle density in the 1D gas. We use the local  $\gamma(z) = mg/n_{\rm 1D}(z)\hbar^2$  in the trapped system.

The number of particles in each 1D gas depends on its (x, y) position, which can be modelled as

$$N(x,y) = N(0,0) \left[ 1 - \frac{x^2 + y^2}{R_{TF}^2} \right]^{3/2},$$
 (2)

where N(0,0) is the number of particles in the central 1D gas and  $R_{\rm TF}$  is the Thomas–Fermi radius<sup>38</sup>. The total number of atoms in the system is  $N_{\rm tot} = \sum_{x,y} N(x,y)$ . With the experimentally measured  $R_{\rm TF}$  and  $N_{\rm tot}$ , we can find N(x,y). The averaged  $\overline{y}$  for the experimental system is defined as

$$\overline{\gamma} = \frac{1}{N_{\text{tot}}} \sum_{x,y} \int n_{\text{1D}}(z;x,y) \gamma(z;x,y) dz.$$
 (3)

 $n_{1D}(z;x,y)$  can be calculated from the Bethe ansatz solution of the homogeneous LL model using the local density approximation and knowledge of N(x,y) and U(z).

#### Momentum and rapidity measurements

To measure momentum distributions, we turn off the 2D lattice and the crossed dipole trap suddenly and let the atoms expand in free space for a time of flight, TOF (TOF = 42 ms for  $\bar{\gamma}$  = 2.3 – 7.6 and TOF = 45 ms for  $\bar{\gamma}_0$  = 0.94), before taking an absorption image<sup>22</sup>. When the 2D lattice

is turned off, the atom cloud expands rapidly in the transverse direction and the energies associated with atom–atom interactions decrease significantly before the momentum distribution can evolve. The initial cloud sizes range from 15 to 25  $\mu m$  for  $\overline{\gamma}_0$  = 0.94to 7.6. The TOF is limited by the transverse expansion that is essential to the momentum measurement  $^{22}$ .

To measure rapidity distributions, we expand the atoms in an approximately flat potential in one dimension until the distribution reaches its asymptotic shape <sup>22,23</sup>. The flat potential is made by leaving a shallow axial trap on to cancel the anti-trap from the blue-detuned lattice. After the Bragg pulse, the rapidity distribution of the central peak does not change on the short timescale of approximately 0.5 ms, before the movement of atoms in the axial trap starts to affect the distribution (Extended Data Fig. 2). The flat potential has a finite size of approximately 40 µm, which means that the rapidity measurement is only accurate for the central peak. The side peaks are distorted, as they fall down the potential hill of the blue-detuned lattice. However, the distortion does not significantly change during the first approximately 0.5 ms of evolution, so the message of Extended Data Fig. 4, that the rapidities do not evolve in this time, is not undermined. We only show rapidities measurements for the condition  $\overline{y}_0 = 2.3$ , because the flat potential is not long enough when  $\bar{y}_0$  is higher and the side peaks are not well enough separated from the central peak when  $\overline{y}_0$  is lower.

#### **Energy error bar**

Each time point in the energy curves of Fig. 3 is obtained from an average of ten images, taken in two groups of five during the experiment. To minimize extra noise associated with background drifts, it is necessary to average at least five images before extracting the energy. We combine the data for these averages in two ways, first by combining the images within each temporally separated group of five and second by combining them into groups of odd and even images. For each grouping approach, we calculate average errors by taking the average over all time points of the root-mean-square difference between the two groups. The grouping makes no difference for the  $\overline{y}_0 = 2.3$  data, but for the other data the average error tends to be higher for the temporally separated groups, which is indicative of small experimental drifts. The average errors calculated using temporally separated groups are higher than the ones calculated using the odd and even group by 86% for the  $\overline{y}_0 = 0.94$  data and 76% for the  $\overline{y}_0 = 3.4$  data. To account for the error associated with the drift, without overstating its contribution to the total error, for all the curves we use the average of the average errors obtained with the two grouping approaches.

#### Time constants from the $p_f$ curves

The shape of the  $p_f(t_{\rm ev})$  curves are not universal (Fig. 4a,b), so they will not all fit to the same simple function. There are two reasons for the differences among these curves. First, there are things that affect the calculated or measured momentum distributions. Theoretically, momentum distributions for different densities are affected differently by particle number effects. Experimentally, high  $\overline{\gamma}_0$  momentum distributions are somewhat broadened by finite-size contributions to the momentum measurements. They are negligible for  $\overline{\gamma}_0 = 0.94$  and become more significant at higher  $\overline{\gamma}_0$ , for which the initial cloud lengths are larger (as large as  $25~\mu m$  for  $\overline{\gamma}_0 = 6.9$ ) and the kinetic energies are smaller. As a check on the importance of this effect, we deconvolved the initial size effects under the assumption that the initial momentum distributions are the theoretical bosonic distributions. We find that the extracted time constants barely change as a result, so we present only the directly measured  $p_f(t_{\rm ev})$ .

The second reason that these curves have different shapes relates to the motion of the side peaks. The  $p_f(t_{\rm ev})$  curves eventually decay from their peak value because the local GGE changes as the side peaks progressively overlap less with the central peak. The effect is larger and faster when the density is higher and the initial cloud length is

smaller, that is, at lower  $\bar{\gamma_0}$  or higher average density. The effect is also evident from the difference between the  $\bar{\gamma_0}$  = 3.4 and 3.7 curves in Fig. 4a, for which the difference in  $\bar{\gamma_0}$  is due to a difference in initial density.

We have tried two ways to extract relatively universal time constants from these varied shape curves. For the first method, which we use in Fig. 4c, we determined the minimum  $(p_{50}^i)$  and maximum  $(p_{50}^e)$  of  $p_{50}$  for the initial rise and find the average of the two,  $(p_{50}^{\rm m} = (p_{50}^{\rm e} + p_{50}^{\rm i})/2)$ . We determine the time at which  $p_{so}^{m}$  is reached by fitting the three nearest to  $p_{50}^{\rm m}$  points to a straight line. The second method was to identify how long it takes to rise from 20% to 80% of the maximum change in  $p_{50}$ , for which those points were determined with local linear fits. Both approaches give similar results for the time constant as a function of  $1/\sqrt{\epsilon}$  (Fig. 4c), with quantitatively comparable linear dependence. We chose to use the first method because it gives somewhat more similar values for the  $\overline{\gamma}_0 = 3.4$  and 3.7 curves, despite their rather different shapes. For  $\overline{y_0} = 0.94$ , 2.3 and 3.4, the  $p_f(t_{ev})$  curves were taken with about three times as many points as at the earliest times. To minimize the effect of fluctuations on the time constants. we smooth the curves by averaging each  $p_f(t_{ev})$  with two neighbouring points. The smoothed curves are then used to extract the time constants.

To calculate the error bars for the time constants, we first find  $\Delta p_{50}^{\rm m}$  by combining in quadrature the errors from determining the minimum and maximum of the  $p_{50}$  ( $\Delta p_{50}^{\rm i}$ ,  $\Delta p_{50}^{\rm e}$ ) with the fitting error associated with the offset from  $p_{50}^{\rm m}$  of the linear fit of the three points near  $p_{50}^{\rm m}$ . We then use the slope of the linear fit line to convert  $\Delta p_{50}^{\rm m}$  to  $\Delta \tau_{p_{50}}$ .

The theoretical time constants plotted in Fig. 4c are extracted as follows. We first smooth the theoretical curve  $\widetilde{\rho}_{50}(t_{\rm ev})$  by averaging each  $p_{50}(t_{\rm ev})$  with its neighbouring points within a time interval  $\delta t_{\rm ev}$ ,  $\widetilde{\rho}_{50}(t_{\rm ev}) = \sum_{t \in [t_{\rm ev} \pm \delta t_{\rm ev}/2]} p_{50}(t)/N_{\delta t_{\rm ev}}$ .  $N_{\delta t_{\rm ev}}$  is the total number of data points used for the average. By choosing  $\delta t_{\rm ev}$  such that it matches the oscillation period for hydrodynamization, we try to minimize its effect on the local prethermalization time constant. Then, as when extracting the experimental time constants, we define the time constant as the time at which  $\widetilde{\rho}_{50}^{\rm m} = (\widetilde{\rho}_{50}^{\rm e} + \widetilde{\rho}_{50}^{\rm i})/2$  is reached. We estimate the error associated with the smoothing procedure to be  $\Delta p_{50}^{\rm m} = \sqrt{\sum_t [p_{50}(t) - \widetilde{\rho}_{50}(t)]^2/(N_{\delta t_{\rm ev}}N_t)}$ . The average is done for  $t \in [t_{30\%}, t_{70\%}]$ , where  $t_{30\%}$  and  $t_{70\%}$  are the times when  $\widetilde{\rho}_{50}$  changes by 30% and 70%, respectively.

#### Tonks-Girardeau limit

We model the TG limit  $(y \rightarrow \infty)$  of the LL Hamiltonian (1) using the low-site-occupancy regime of the lattice hard-core boson Hamiltonian,

$$\mathcal{H}_{HCB} = -J \sum_{j=1}^{L-1} (\hat{b}_{j+1}^{\dagger} \hat{b}_{j} + \text{h.c.}) + \sum_{j=1}^{L} U(z_{j}) \hat{b}_{j}^{\dagger} \hat{b}_{j},$$
 (4)

where h.c. denotes the Hermitian conjugate, J is the hopping amplitude and L is the total number of lattice sites.  $\hat{b}_j^{\dagger}$  and  $\hat{b}_j$  create and annihilate, respectively, a hard-core boson at site j, with the additional constraints  $\hat{b}_j^{\dagger 2} = \hat{b}_j^{\dagger 2} = 0$  to enforce the hard-core condition. The position of site j in the lattice is taken to be  $z_j = (j-L/2)a$ , where a is the lattice spacing. In the limit of vanishing site occupancy  $(n_j = \langle \hat{b}_j^{\dagger} \hat{b}_j \rangle \rightarrow 0$  at all sites), in which the average distance between particles is much larger than a, the lattice Hamiltonian (4) is equivalent to the continuum TG limit of the LL Hamiltonian (1) (refs. 22,39.). The parameters of the two Hamiltonians satisfy the relation  $J = \hbar^2/(2ma^2)$ .

The momentum distributions studied experimentally are, up to a normalization constant,

$$f(p,t) \propto \langle \Psi(t) | \hat{b}_{p}^{\dagger} \hat{b}_{p} | \Psi(t) \rangle = \sum_{jl} e^{ip(z_{j}-z_{l})/\hbar} \langle \Psi(t) | \hat{b}_{j}^{\dagger} \hat{b}_{l} | \Psi(t) \rangle, \quad (5)$$

where  $\hat{b}_p^{\dagger}$  and  $\hat{b}_p$  create and annihilate, respectively, a hard-core boson at momentum p, and  $|\Psi(t)\rangle$  is the time-evolving state.

The one-body correlations  $\langle \Psi(t)| \hat{b}_j^{\mathsf{T}} \hat{b}_i | \Psi(t) \rangle$  of the 1D lattice hard-core bosons can be computed exactly by mapping the hard-core boson Hamiltonian onto non-interacting spinless fermions via the Jordan–Wigner transformation, which yields<sup>40</sup>

$$\langle \Psi(t)|\hat{b}_{j}^{\dagger}\hat{b}_{l}|\Psi(t)\rangle = \langle \Psi(t)|\hat{c}_{j}^{\dagger}\hat{S}_{j-l}\hat{c}_{l}|\Psi(t)\rangle,$$
where  $\hat{S}_{j-l} = \exp\left[i\pi \sum_{m=\min(j,l)}^{\max(j-1,l-1)} \hat{c}_{m}^{\dagger}\hat{c}_{m}\right].$  (6)

The 'string operator'  $\hat{S}_{j-l}$  'counts' fermion number fluctuations between positions  $z_j$  and  $z_h$ , and we note that  $|\Psi(t)\rangle$  was written in the main text in terms of fermion creation operators in rapidity space,  $\hat{c}_{\theta}^{\dagger}$ . Recall that  $\hat{c}_{\theta}^{\dagger} = \sum_{i} e^{i\theta z_i/\hbar} \hat{c}_{i}^{\dagger}$ .

Plugging equation (6) in equation (5), one can see that f(p,t) is dominated by the non-local real-space correlation function  $C(\ell_p,t)$ , namely, that  $f(p,t) \approx C(\ell_p,t)$ , where  $C(\ell_p,t) \equiv \sum_j \langle \Psi(t) | \hat{c}_j^\dagger \hat{S}_{\ell_p/a} \hat{c}_{j+\ell_p/a} | \Psi(t) \rangle$  involves the quantum fluctuations in the number of fermions over a length scale  $\ell_p = 2\hbar\pi/p$ .  $C(\ell_p,t)$  is the non-local real-space correlation function mentioned in the main text in the context of the theoretical discussion about local prethermalization.

Exact numerical calculations of equation (5) are carried out using properties of Slater determinants  $^{39,41}$ . For the ground-state calculations, we choose the lattice spacing to be  $a=5\times10^{-9}$  m and simulate systems with up to L=12,000 lattice sites. We verify that lattice effects are negligible by doing some of the calculations on a lattice with twice as large a and checking that the results do not change within the desired accuracy. Owing to the much higher computational cost of the finite-temperature calculations  $^{41}$ , the finite-temperature data presented in Extended Data Figs. 5 and 9 were obtained for  $a=3.2\times10^{-8}$  m ( $a=4\times10^{-8}$  m) on a lattice with L=1,500 sites for T=5 nK (10 nK).

Our numerical calculations start at t = 0 from the ground (or finite-temperature) state of equation (4) with N particles and a Gaussian-shaped trapping potential

$$U(z) = U_0 \left[ 1 - \exp\left(-\frac{2z^2}{W^2}\right) \right],$$
 (7)

where  $U_0$  is the strength of the Gaussian trap and W is the trap width. As in the experiments, the quench is implemented by evolving the initial state under Hamiltonian (4) with the addition of the Bragg pulse potential (characterized by an amplitude  $U_{\rm pulse}$  and a wave number k)

$$U_{\text{pulse}}(z) = U_{\text{pulse}}\cos^2(kz), \tag{8}$$

for a time  $t_{\rm pulse}$ . At times  $t=t_{\rm pulse}+t_{\rm ev}$ , the system evolves under the initial Hamiltonian (7), and it is during those times that we calculate the momentum and rapidity distributions. For Figs. 1 and 3 and Extended Data Figs. 1, 3, 5, 6 and 9, we use  $t_{\rm pulse}=6~\mu \rm s$ , as in the experiment. Figure 4 and Extended Data Figs. 8c, d all use  $k=4k_0$  to shorten the hydrodynamization timescale relative to the local prethermalization timescales. To minimize many-body evolution during the Bragg pulse, we decrease  $t_{\rm pulse}$  to 1  $\mu \rm s$  in those calculations, while increasing  $U_{\rm pulse}$  to keep the fraction of atoms in the central peak fixed.

## **Data availability**

The data for all the figures can be found at https://doi.org/10.7910/DVN/KFGNRH. Source data are provided with this paper.

- Kinoshita, T., Wenger, T. & Weiss, D. S. All-optical bose-einstein condensation using a compressible crossed dipole trap. Phys. Rev. A 71, 011602 (2005).
- Olshanii, M. Atomic scattering in the presence of an external confinement and a gas of impenetrable bosons. Phys. Rev. Lett. 81, 938–941 (1998).
- Yang, C. N. & Yang, C. P. Thermodynamics of a one-dimensional system of bosons with repulsive delta-function interaction. J. Math. Phys. 10, 1115–1122 (1969).

- Tolra, B. L. et al. Observation of reduced three-body recombination in a correlated 1D degenerate bose gas. Phys. Rev. Lett. 92, 190401 (2004).
- Rigol, M. & Muramatsu, A. Ground-state properties of hard-core bosons confined on one-dimensional optical lattices. Phys. Rev. A 72, 013604 (2005).
- Cazalilla, M. A., Citro, R., Giamarchi, T., Orignac, E. & Rigol, M. One dimensional bosons: from condensed matter systems to ultracold gases. Rev. Mod. Phys. 83, 1405–1466 (2011)
- 41. Xu, W. & Rigol, M. Expansion of one-dimensional lattice hard-core bosons at finite temperature. *Phys. Rev. A* **95**, 033617 (2017).

**Acknowledgements** We acknowledge N. Malvania for preliminary experimental work related to this paper. This work was supported by NSF grants PHY-2012039 (D.S.W., Y.L. and Y.Z.), PHY-2012145 (Y.Z. and M.R.) and DMR-1653271 (S.G.). The computations were carried out at the Institute for Computational and Data Sciences at Penn State University.

**Author contributions** Y.L. carried out the experiments and experimental analysis. Y.Z. carried out the theoretical calculations. D.S.W. oversaw the experimental work. M.R. and D.S.W. oversaw the theoretical work. Y.L., Y.Z, S.G, M.R. and D.S.W were all involved in the analysis and interpretation of the results, and all contributed to writing the paper.

Competing interests The authors declare no competing interests.

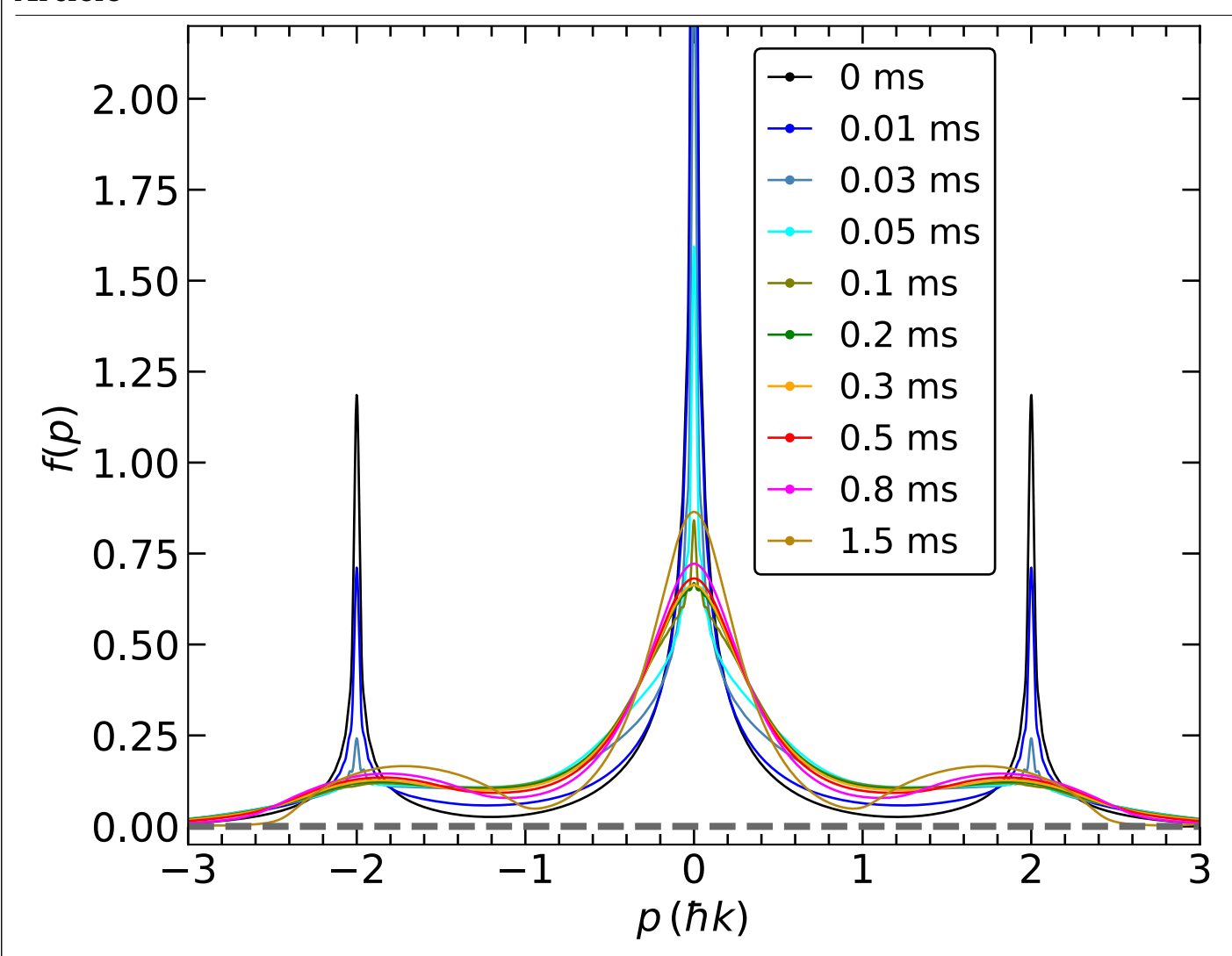
#### Additional information

**Supplementary information** The online version contains supplementary material available at https://doi.org/10.1038/s41586-023-05979-9.

Correspondence and requests for materials should be addressed to David S. Weiss.

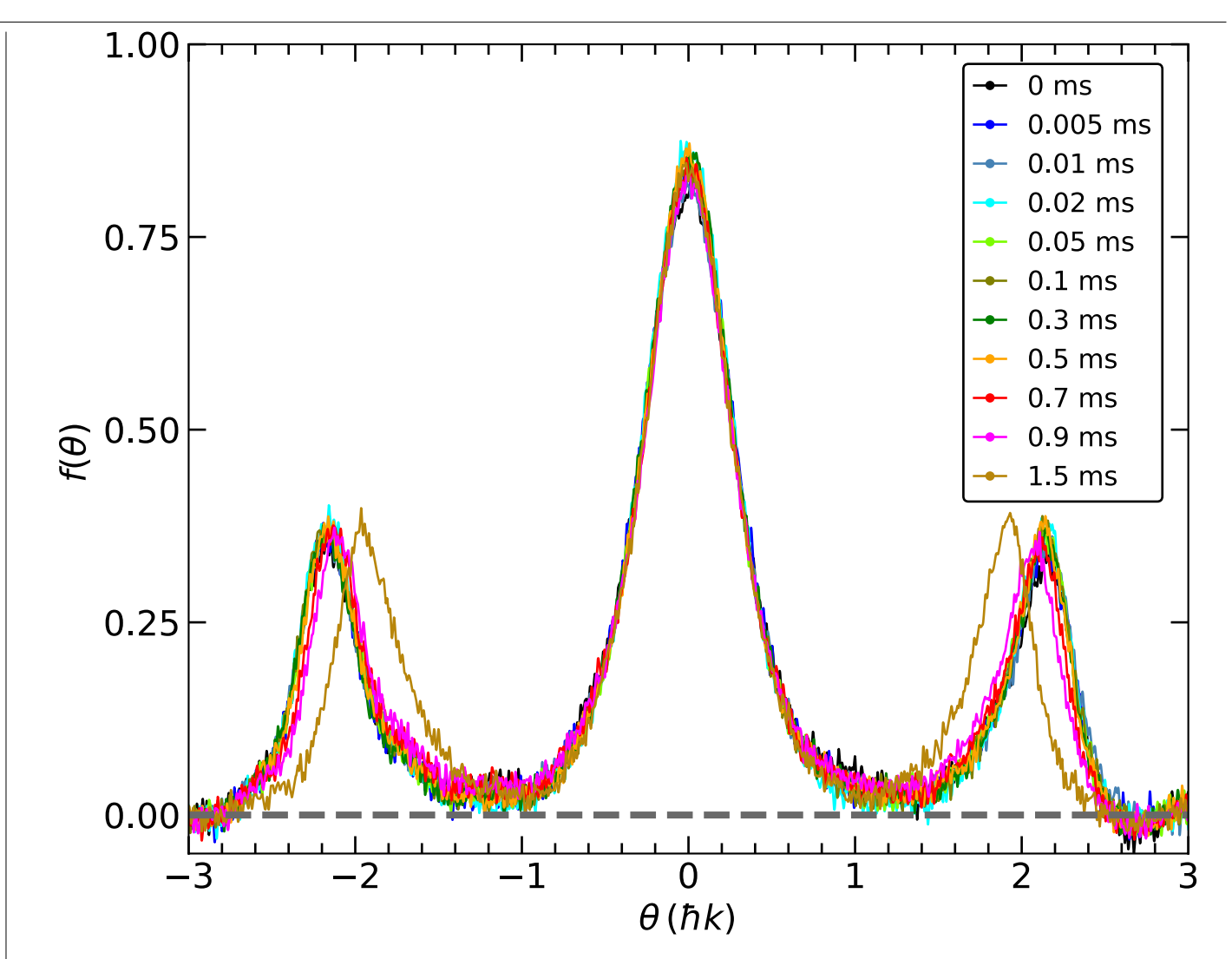
Peer review information Nature thanks the anonymous reviewers for their contribution to the peer review of this work.

Reprints and permissions information is available at http://www.nature.com/reprints.



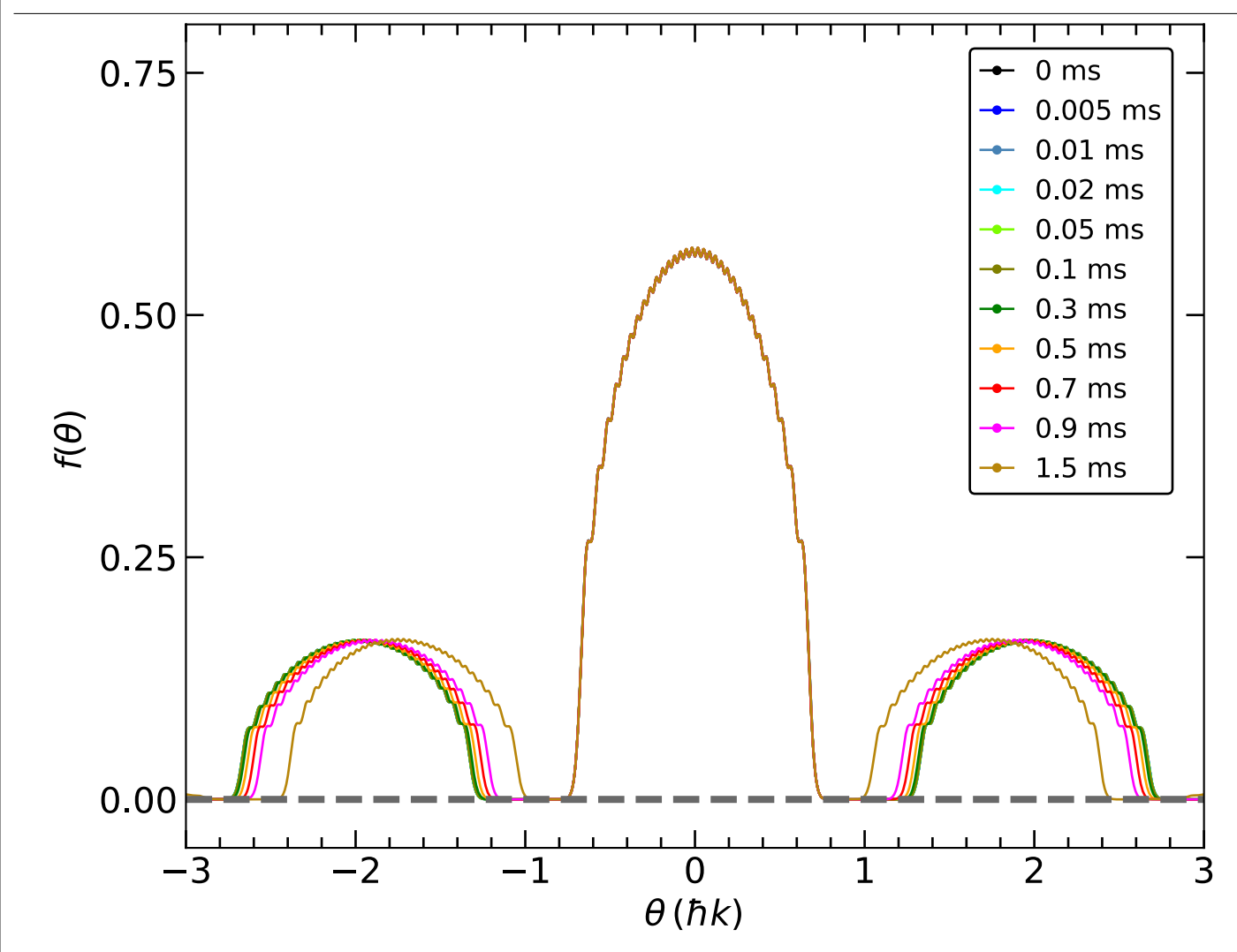
**Extended Data Fig. 1**| **Theoretical momentum distributions.** Calculations are done for a single 1D tube in the TG limit at zero temperature. We use the same trap and quench parameters as in the  $\bar{\gamma}_0$  = 2.3 experiment, and choose the atom

number in the tube to be N=32 in order to match the experimental average energy density. These curves match the experimental evolution times in Fig. 1.



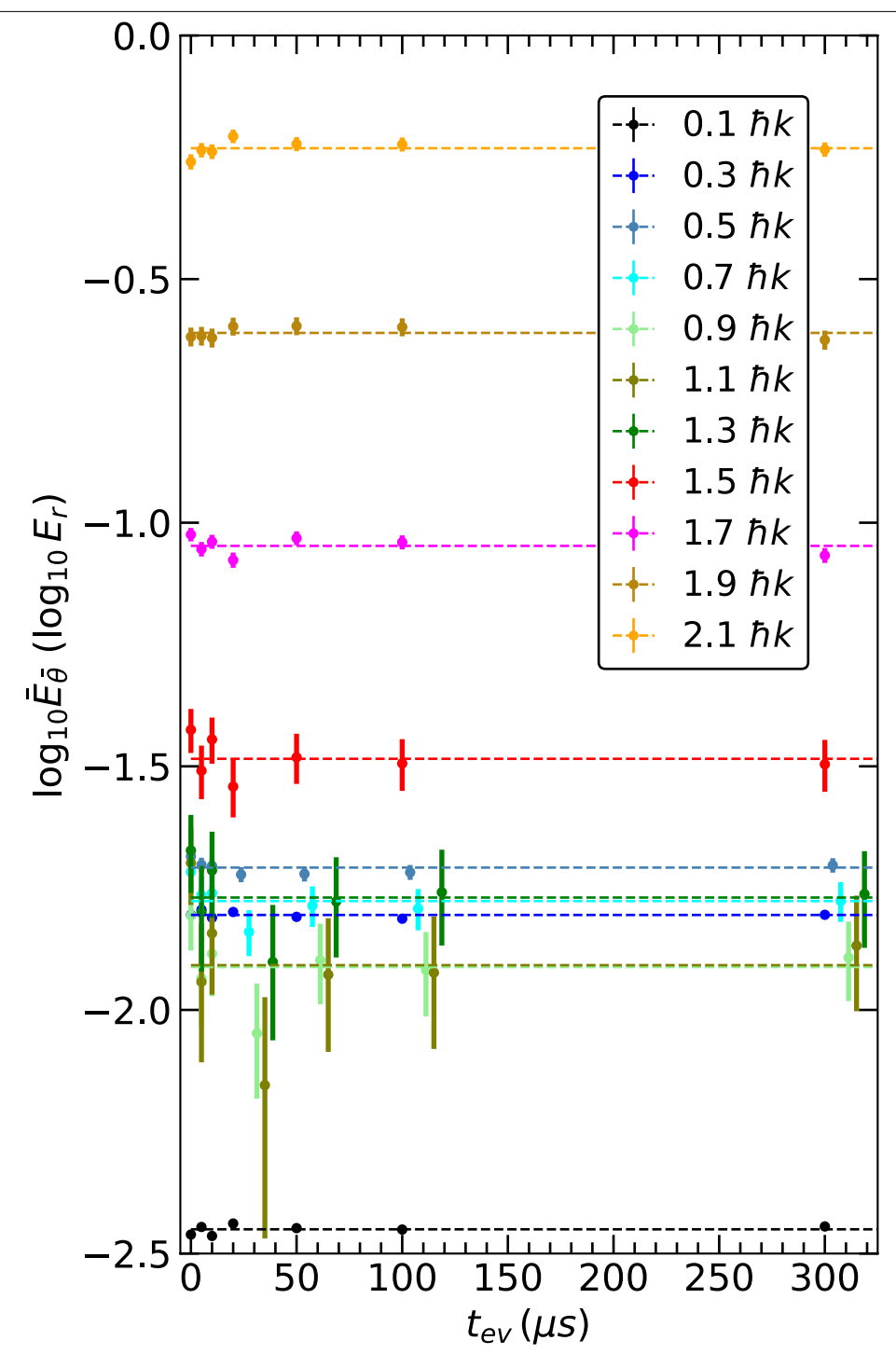
**Extended Data Fig. 2** | **Experimental rapidity distributions for**  $\overline{\gamma}_0$  = **2.3 at a sequence of times after the Bragg scattering quench.** The central part of the rapidity distribution does not appreciably change over 1.5 ms, which is less than 10% of the trap oscillation period. The rapidities measurement for the side peaks are slightly distorted by the fact that the flat potential does not extend far enough for atoms moving that fast (after they have moved approximately

 $20\,\mu\text{m}$ , they are accelerated slightly). Still, since the distortion is approximately the same for all times within the first approximately 0.5 ms, the fact that the measured distribution does not change implies that that part of the rapidity distribution also remains constant. After approximately1 ms, the side peaks start to be noticeably slowed as they climb up the potential of the Gaussian axial trap.



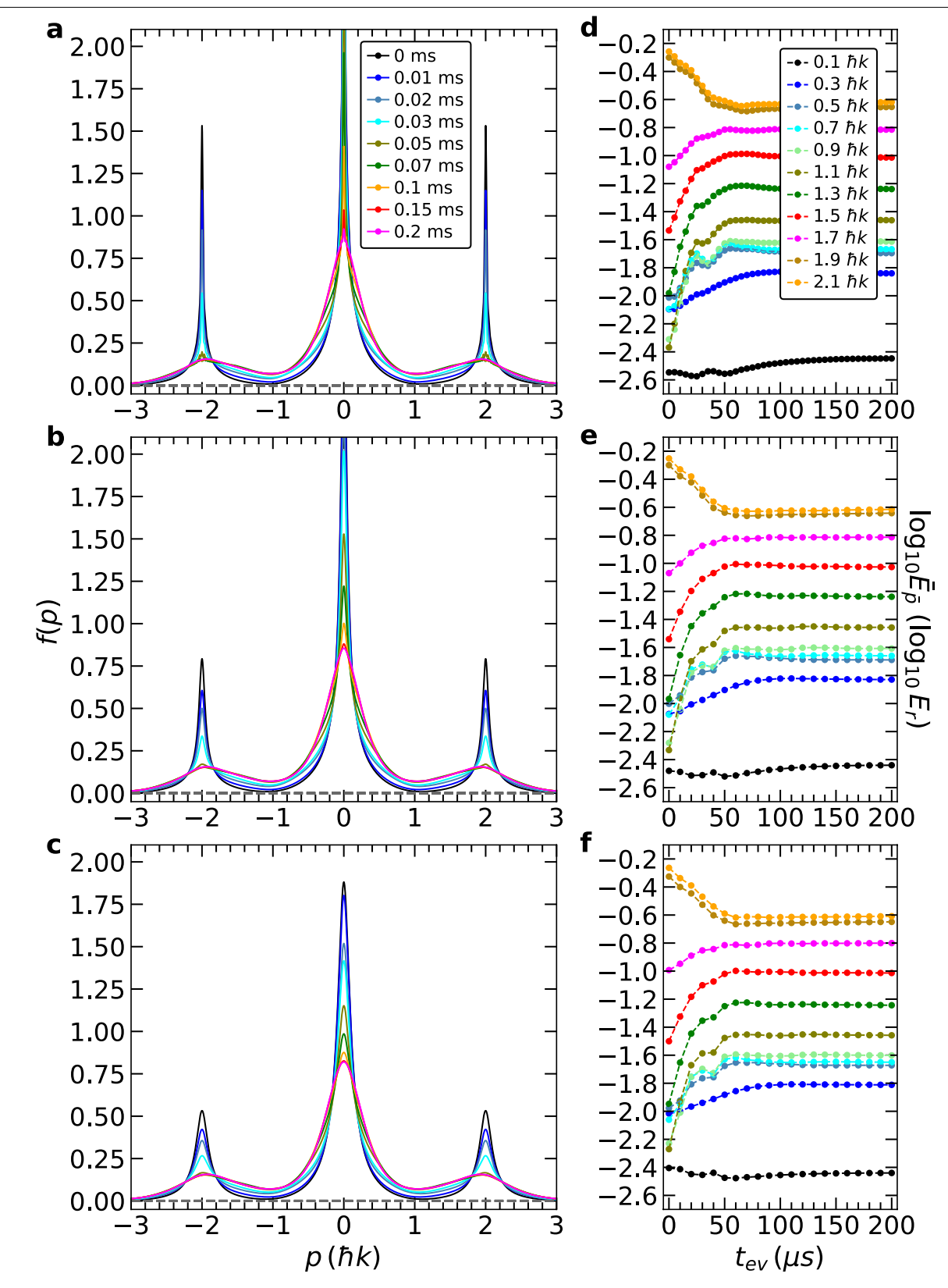
**Extended Data Fig. 3** | **Theoretical rapidity distributions.** These simulations are done for a single 1D tube in the TG limit at zero temperature with same trap and quench parameters as in the  $\overline{y_0} = 2.3$  experiment. The atom number in the

tube is chosen to be N=32 in order to match the experimental average energy density. These curves match the experimental evolution times of Extended Data Fig. 2.



**Extended Data Fig. 4** | **Integrated experimental rapidity energy.** The curves are extracted from the rapidity profiles for  $\bar{\gamma_0}$  = 2.3 integrating over different 0.2  $\hbar k$  wide rapidity groups. The different colours denote different rapidity groups (as in Fig. 3), defined in the key. For the average rapidity  $\bar{\theta}$  = 0.5  $\hbar k$  - 1.3  $\hbar k$  curves, we have horizontally shifted the points for times longer than  $t_{ev}$  = 20  $\mu$ s

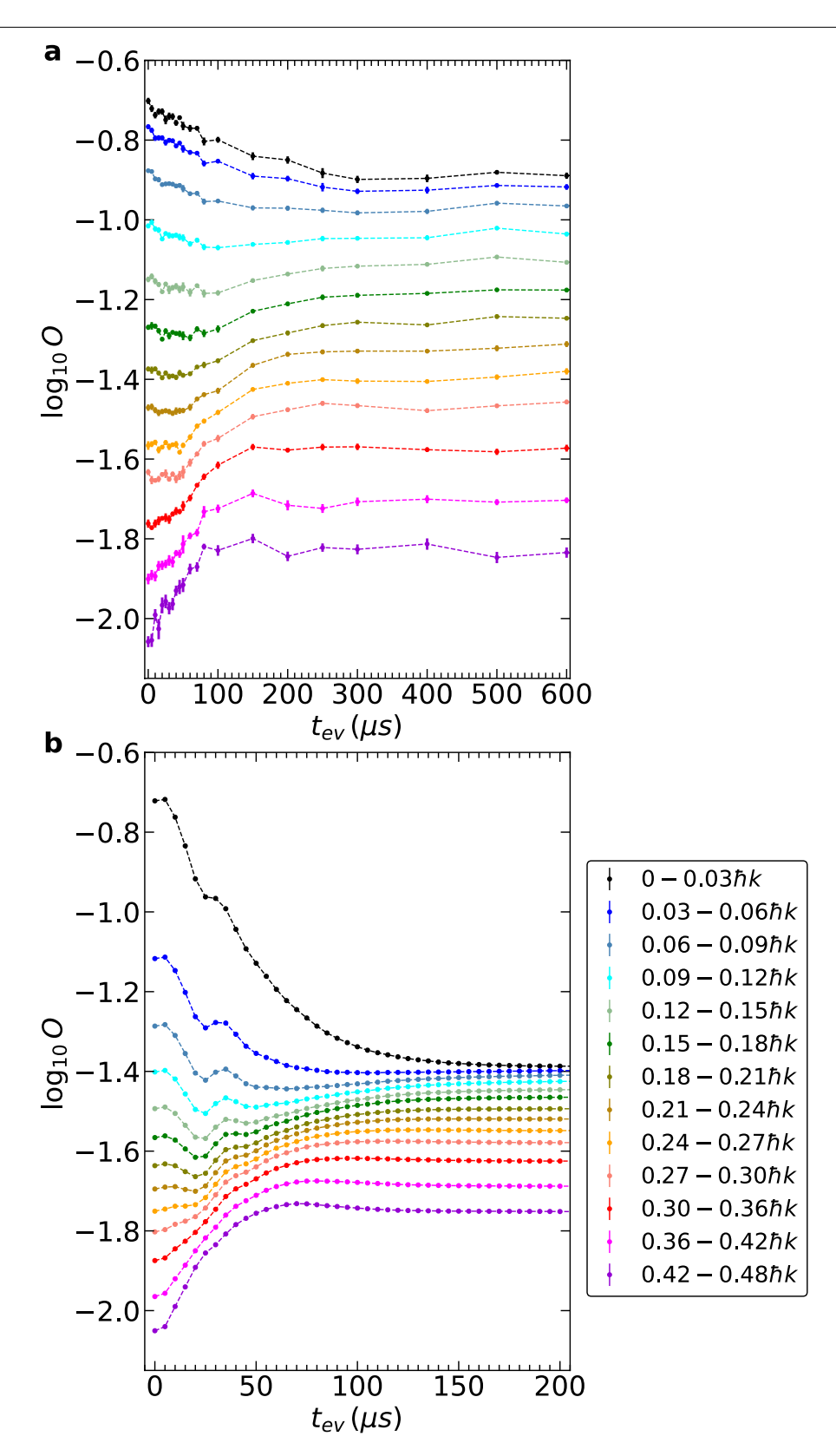
in order to better resolve the different rapidity group energies at the same time. The dashed lines show the average energy for each rapidity group. There is no detectable change in the energy of each rapidity group in the first approximately  $300\,\mu s$ , in stark contrast to the 3 dB-scale rapid changes in the energies associated with momentum groups in Fig. 3b.



**Extended Data Fig. 5** | See next page for caption.

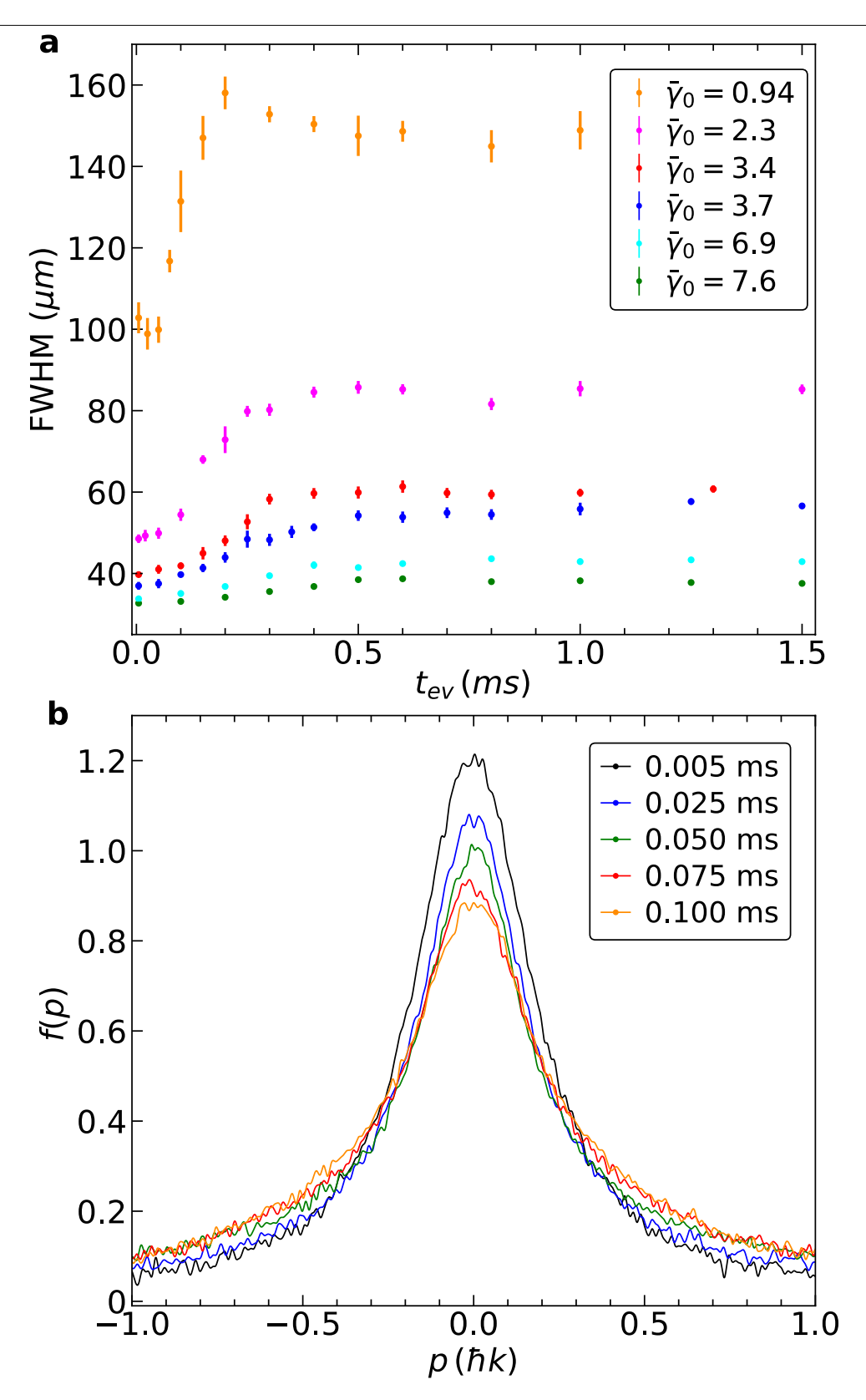
**Extended Data Fig. 5** | **Effect of finite temperature on momentum distributions and integrated kinetic energy.**  $\mathbf{a}$ - $\mathbf{c}$ , Theoretical momentum distributions for a single 1D tube in the TG limit at 0 nK, 5 nK and 10 nK, respectively (see Methods). We use the same trap and quench parameters as in the  $\overline{y}_0$  = 3.4 experiment, and choose the atom number in the tube to be N = 29 to match the experimental average energy density. These temperatures are the highest we expect there to be in the experiment. One can see that the effect is mostly to smooth out the sharp peaks. Note also that similar smoothing also results from finite time-of-flight in the experiment [24].  $\mathbf{d}$ - $\mathbf{f}$ , Corresponding

theoretical integrated kinetic energy at 0 nK, 5 nK and 10 nK, respectively. Each curve shows the time evolution of the integrated energy in a different  $0.2\hbar k_0$  wide momentum group. Curves in the same momentum group have very similar shapes at zero and finite temperatures. Since hydrodynamization involves a much larger energy scale than that associated with these temperatures, it is not surprising that temperature does not significantly affect the signatures of hydrodynamization. We conclude that the differences between the experimental and theoretical results in Fig. 3 are not a result of finite temperature effects.



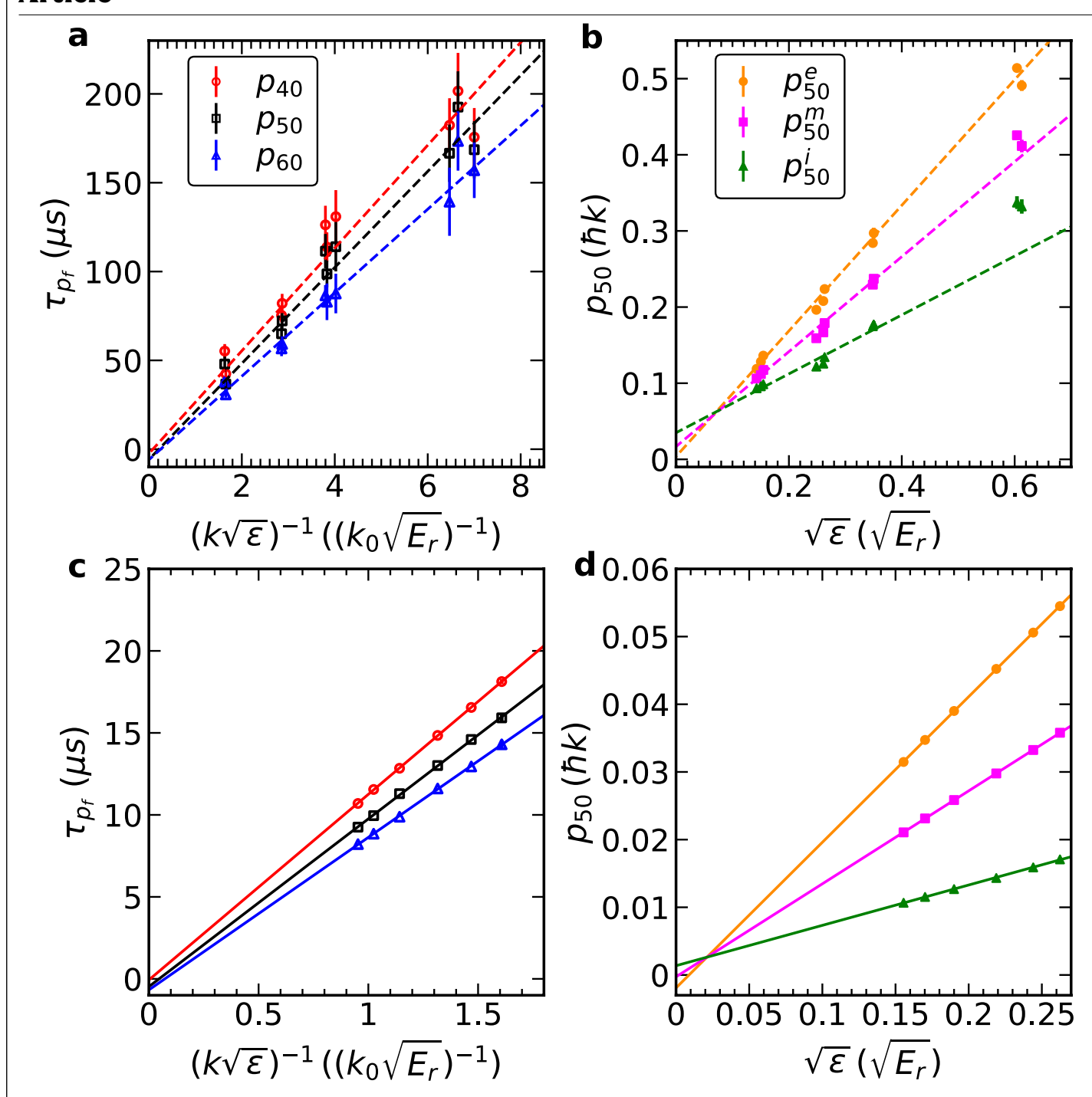
**Extended Data Fig. 6** | The time evolution of the occupations (*O*) of different momentum groups within the central peak. **a**, Experimental curves for  $\bar{\gamma_0} = 2.3$  are plotted on a log scale. Each curve is obtained by integrating the area of the normalized momentum distribution within the designated momentum range. Different colours denote the different momentum groups as shown in the legend. The last three momentum groups,  $0.30 - 0.36 \, \hbar k$ ,  $0.36 - 0.42 \, \hbar k$ , and  $0.42 - 0.48 \, \hbar k$ , have twice the integration range, so their occupations are divided by 2. **b**, Theoretical curves for a single 1D gas in the TG limit with the

same average energy as in the experiment with  $\overline{y_0}=2.3$ . In both the experiment and the theory, the occupation of higher momentum groups evolves faster than the lower ones, as expected for local prethermalization. The fact that each of these curves has a different shape makes it difficult to quantitatively compare time constants among them. The theoretical curves evolve more than twice as fast as the experimental curves, presumably reflecting the difference between infinite and finite g (see Eq. (1)).  $k=k_0$  for the experiment and  $k=4k_0$  for the theory.



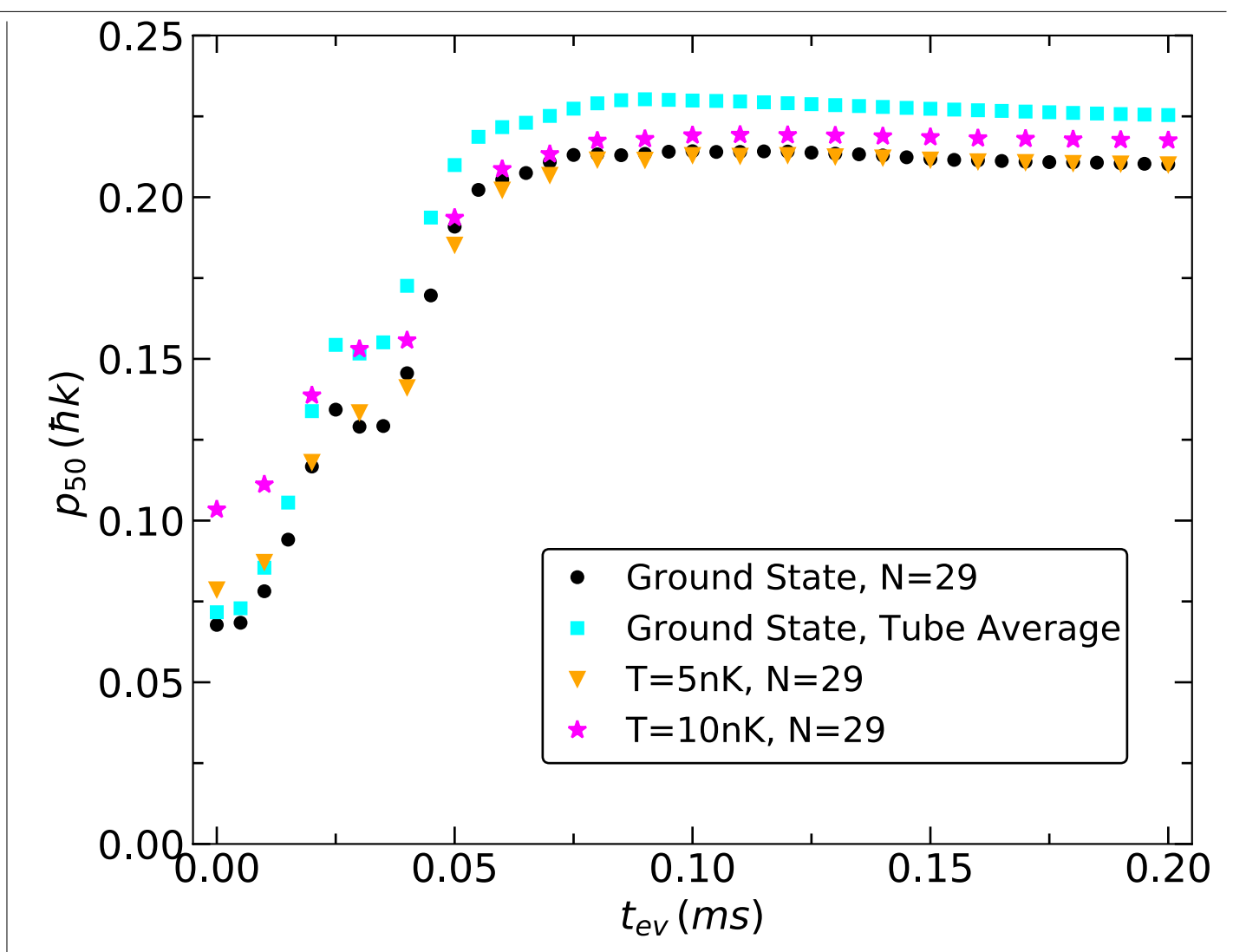
**Extended Data Fig. 7** | **Time evolution of the FWHM. a**, The evolution of the FWHM of the central peak in the momentum distributions after the Bragg scattering quench for different coupling strengths. To a greater degree than for the  $p_{50}(t_{ev})$  curves of Fig. 3, these curves all have different shapes. **b**, The evolving momentum distribution of the central peak for  $\overline{y_0} = 0.94$ . These curves

correspond to the first five points of the orange curve in  ${\bf a}$ . The momentum distribution clearly evolves during the first 0.05 ms, even though the FWHM does not change. This illustrates that the FWHM is not a reliable marker of the evolution of these momentum distributions.



**Extended Data Fig. 8** | **Relationships among**  $p_p$ ,  $\tau_{p_p}$ , and  $\epsilon$ . a, Experimental time constants associated with  $p_{40}$  (red circles),  $p_{50}$  (black squares), and  $p_{60}$ (blue triangles) as functions of  $1/k\sqrt{\epsilon}$ . As in all the experiments presented in this paper, k is fixed at  $k_0$ . The time constants are extracted from curves like those in Fig. 4a (see Methods). The dashed lines are least-squares linear fits; the intercepts are  $-2.5 \pm 5.6$ ,  $-5.8 \pm 4.9$ ,  $-6.0 \pm 3.5$  for  $p_{40}$ ,  $p_{50}$ , and  $p_{60}$ , respectively. The data are consistent with linear relationships between the time constant associated with each  $p_f$  and the inverse of the square root of average energy per particle. For a given momentum distribution, the actual values of  $p_{40}$  and  $p_{60}$ span a range of  $\sim \pm 30\%$  around the steepest part of the distribution (at  $\sim p_{50}$ ). **b**, Experimental  $p_{50}$  vs  $\sqrt{\epsilon}$ . The green triangles, magenta squares, and orange circles correspond to the initial  $(p_{50}^i)$ , middle  $(p_{50}^m)$ , and final  $(p_{50}^e)$  values of  $p_{50}$ for each experimental condition, extracted from Fig. 4a. The dashed lines are least-squares linear fits; the intercepts are  $(3.5 \pm 0.9) \times 10^{-2}$ ,  $(1.7 \pm 0.6) \times 10^{-2}$ , and  $(3.8 \pm 4.4) \times 10^{-3}$  for  $p_{50'}^i, p_{50'}^m$  and  $p_{50'}^e$ , respectively. The  $p_{50}^i$  points at the lowest  $\epsilon$  (highest  $\overline{y}_0$ ) conditions are more likely to be affected by finite-size

corrections to their momentum distributions. The data show a linear relationship between each measured value and  $\sqrt{\varepsilon}$ .  $\mathbf{c}$ , Theoretical time constants obtained from the  $p_{40}$ ,  $p_{50}$ , and  $p_{60}$  curves simulated with  $k=4k_0$ . The time constants are obtained from curves like those in Fig. 4b. The error bars are smaller than the marker size. The solid lines are least-squares linear fits; the intercepts are  $-0.065\pm0.047$ ,  $-0.47\pm0.13$ , and  $-0.67\pm0.10$  for  $p_{40}$ ,  $p_{50}$ , and  $p_{60}$ , respectively.  $\mathbf{d}$ , Theoretical  $p_{50}$  vs  $\sqrt{\varepsilon}$ , simulated with  $k=4k_0$ . The intercepts are  $(14\pm1.3)\times10^{-4}$ ,  $(2.7\pm0.53)\times10^{-4}$ , and  $(-19\pm1.2)\times10^{-4}$ , for  $p_{50}^i$ ,  $p_{50}^m$ , and  $p_{50}^e$ , respectively. The momentum feature that is most clearly proportional to  $\sqrt{\varepsilon}$  is  $p_{50}^m$ . Since that is the midpoint value of  $p_{50}$  during the evolution, it is likely to be close to  $\overline{p}_{50}$ , the effective momentum to which the  $p_{50}$  measurement is sensitive. Taken all together, this figure shows that, for  $p_{50}$ , the time constants are proportional to  $1/\sqrt{\varepsilon}$ , which is in turn proportional to the characteristic momentum being measured. We have repeated the entire analysis for  $p_{40}$  and  $p_{60}$  and the conclusions are the same.



**Extended Data Fig. 9** | **Effect of the average over 1D gases and of finite temperature on**  $p_{50}$ . We plot theoretical simulations of  $p_{50}$  in the TG limit with the same trap and quench parameters as in the  $\overline{y_0}$  = 3.4 experiment. For the average over 1D gases, we use the Thomas-Fermi distribution with experimentally measured  $R_{\rm TF}$  = 23  $\mu$ m and a total particle number of  $N_{\rm tot}$  = 2.75 × 10 $^5$  (see Methods). To simplify the calculations, we round the particle number in each tube in steps of 5. The circles show the results of ground state simulations for a single tube with N = 29 particles (which matches the

experimental average energy density). The squares show the results of ground state simulations after averaging over all the 1D gases, as occurs in the experimental setup. The triangles (stars) show simulations for a single tube with N=29 particles at a temperature of T=5 nK (10 nK). We did the finite temperature simulations with a larger discretization  $a=3.2\times10^{-8}$  m ( $a=4\times10^{-8}$  m) due to numerical limitations (see Methods). The results show no significant changes in the time constant due to either the average over tubes or finite temperature.